

**Removing the effects of free-surface from seismic data using
convolutional neural networks – Part 2: An application to
the Mobil AVO Viking Graben data set**

Mert S. R. Kiraz^{†,‡}, *Roel Snieder*[†] & *Jon Sheiman*

[†] *Center for Wave Phenomena, Colorado School of Mines, Golden CO 80401, USA*

[‡] *Corresponding author*

E-mail: mertkiraz@gmail.com; rsnieder@mines.edu; jonsheiman1@gmail.com

(January 19, 2023)

CWP-1009

Running head: **Removing the effects of free-surface using CNNs: the Mobil
AVO Viking Graben data set**

ABSTRACT

The presence of the air-water interface (or free-surface) creates two major problems in marine seismic data; free-surface multiples and ghost reflections. The attenuation of free-surface multiples remains one of the most challenging noise attenuation problems in seismic data processing. Current solutions suffer from the removal of the primary event along with the multiple events especially when the primary and multiple events overlap (e.g., adaptive subtraction). The effective attenuation of ghost reflections (or *deghosting*) requires acquisition- and/or processing-related solutions which generally address the source-side and receiver-side ghosts separately. Additionally, an essential requirement for a successful implementation of free-surface multiple attenuation and deghosting is the requirement of dense seismic data acquisition parameters which is not realistic for 2D and/or 3D marine cases. We present a convolutional neural network (CNN) approach for free-surface multiple attenuation and for seismic deghosting, simultaneously. Unlike the existing solutions, our approach operates on a single trace at a time, and neither relies on the dense acquisition parameters nor requires a subtraction process to eliminate free-surface multiples, and it removes both the source ghost and receiver ghost simultaneously. We illustrate the efficacy of the free-surface multiple attenuation and seismic deghosting technique using the Mobil AVO Viking Graben field data set. The application of our algorithm demonstrates that our CNN-based approach removes different orders of free-surface multiples (e.g., 1st and 2nd orders) and recovers the low-frequency content of the seismic data (which is essential for, for instance, full-waveform inversion applications and broadband processing) by successfully removing the ghost reflections while preserving and increasing the continuity of the primary reflections.

INTRODUCTION

The occurrence of multiples arises when waves interact with a strong impedance contrast. In marine seismic data, the free-surface (or air-water interface) and water bottom are the two main impedance contrasts. Although the water bottom can be soft (e.g., weak impedance contrast) depending on the geology of the area, the free-surface always is a perfect reflector (e.g., strong impedance contrast). This strong impedance contrast creates two main issues in the recorded seismic data; free-surface multiples and ghost reflections.

Free-surface multiples have at least one downward reflection at the free-surface and are the most dominant set of multiples in marine seismic data. Free-surface multiples can have different numbers of orders which define the multiples' number of bounces from the free-surface. With a higher number of orders, free-surface multiples become harder to attenuate later during the processing stage. Figure 1 shows an example of a 1st-order free-surface multiple (black line). The red star in Figure 1 denotes the source location at depth and the white triangle denotes the receiver location at depth. One of the widely used techniques to address free-surface multiples is called surface-related multiple elimination (SRME) (Verschuur et al., 1992). This technique effectively predicts and iteratively subtracts the multiples (also known as adaptive subtraction) from the seismic data but does not always guarantee perfect solutions. During the subtraction step, the primary reflections might be removed from the seismic data along with the unwanted multiple reflections because of the overlapping primary and multiple events. Additionally, with a complex subsurface, SRME techniques fall short and require dense spatial distribution of source and receiver distribution (Dragoset et al., 2010). This condition becomes even more difficult to fulfill in 3D surveys.

[Figure 1 about here.]

Ghost reflections create notches in the frequency content of the seismic data through destructive interference (Amundsen and Zhou, 2013). It is important to attenuate the effects of ghost reflections, especially for broadband data processing and full-waveform inversion applications (Tarantola, 1984; Plessix, 2006; Kragh et al., 2010). The ghost reflections are recorded in the seismic data as the delayed version of the primary seismic signal with an opposite polarity (Dondurur, 2018). There are three types of ghost reflections that are present in the seismic data; source ghost, receiver ghost, and source & receiver ghost. Figure 1 shows an example of the source & receiver ghost reflection (red line). Removing the ghost reflections from seismic data (or *deghosting*) is mainly performed in two different categories; acquisition-based solutions and processing-based solutions. Acquisition-based solutions include, but not limited to, slanted streamer acquisition (Soubaras and Whiting, 2011), over/under streamer acquisition (Moldoveanu et al., 2007), and dual-sensor streamer acquisition (Carlson et al., 2007). Processing-based solutions include, but not limited to, deriving a low-frequency deghosting filter (Amundsen and Zhou, 2013), and joint deconvolution (Soubaras, 2010). Recently, Hu et al. (2019), Almuteri and Sava (2021), and Vrolijk and Blacquièrre (2021) have also utilized machine learning applications for removing ghost reflections from seismic data.

Seismic migration techniques assume that the input data only contain primary reflections and an example of a primary reflection is shown in Figure 1 (blue line). Therefore, it is imperative for the seismic data to be free from the events caused by the presence of free-surface (red and black lines in Figure 1). We propose a CNN-based solution that is designed to remove the effects of free-surface, namely, attenuating the free-surface multiples

and seismic deghosting, simultaneously. We only use synthetic data set for training and make predictions using the field data set. We first introduce the CNN architecture we use in Section 2, then we illustrate the effectiveness of our CNN-based solution with a 2D Mobil AVO Viking Graben field data set acquired in the North Viking Graben (Keys and Foster, 1998) in Section 3. The application of our CNN algorithm to field data demonstrates that we can attenuate free-surface multiples and remove ghost reflections simultaneously from the seismic data using the CNN. The CNN-based solution we propose requires neither dense source/receiver distribution nor is affected by the missing traces in the recorded data. We also show that during the simultaneous multiple attenuation and seismic deghosting using CNNs, primary reflections have been preserved and their continuity has been increased.

CNN ARCHITECTURE AND TRAINING

Recently, different machine learning (ML) and/or convolutional neural network (CNN) methods have been proposed to attenuate free-surface multiples or remove ghost reflections from seismic data (Siahkoochi et al., 2018, 2019; Hu et al., 2019; Ovcharenko et al., 2021; Zhang et al., 2021; Liu-Rong et al., 2021; Almuteri and Sava, 2021; Vrolijk and Blacquière, 2021). In this paper, we propose a CNN that predicts a single trace at a time, making our algorithm insensitive to the data gaps in the acquisition and does not require a meticulous data-filling pre-processing step, unlike the current techniques.

CNN is a subset of ML and is based on the mathematical and statistical methods that let machines and computers improve specified tasks with experience (Bishop, 2006; Géron, 2019; Ekman, 2021). CNNs consist of layers of filters and as the number of layers increases, the network extracts more complex information, and the networks with many layers are called “deep neural networks”. Every sample in a layer is called a neuron and the output

value of a neuron is obtained by

$$a_j^k = \sigma \left(\sum_{i=1}^N (a_i^{(k-1)} w_{ij}^k) + b_j^k \right), \quad (1)$$

where N denotes the number of neurons in the previous layer, a_j^k denotes the value a to be calculated of the j th neuron in the k th layer, $a_i^{(k-1)}$ denotes the value a of the i th neuron in the $(k-1)$ th layer, w_{ij}^k denotes the weight w of the i th neuron which is connected to the j th neuron in the k th layer, b_j^k denotes the bias b of the j th neuron in the k th layer, and σ denotes the activation function. The activation function is a nonlinear function so that the action of the neural network is nonlinear as well.

The process in which we adjust the weights, w , and biases, b , by an iterative data-fitting process is called training. During the training, once an output of a network is obtained, we define an error function to compare the output of the network to the desired output. The most commonly used error function is the mean-squared error (MSE) metric that measures the difference between the predicted and the ground truth results,

$$MSE = \frac{1}{m} \sum_{i=1}^m (\hat{y}_i - y_i)^2, \quad (2)$$

where \hat{y}_i is the output of the network, y_i is the ground truth data for a given input data during the training, and m is the number of training examples. We minimize the MSE function by using the gradient descent method by calculating the gradient of the error function with respect to the weights. Training a CNN is commonly done by backpropagation where the choice loss function and gradient descent optimization algorithm are essential (Bishop, 2006; Géron, 2019; Ekman, 2021).

In this study, we use the network architecture proposed by Kiraz et al. (2023) for simultaneous free-surface multiple attenuation and deghosting. Our CNN architecture consists of an input layer, 9 1D convolutional layers, and an output layer. The first and second,

fourth and fifth, and seventh and eighth layers have 32 filters (Géron, 2019; Kiraz et al., 2023); the third, sixth, and ninth layers have 8 filters. The length of the 1D convolutional window for the first 3 layers is 1110 samples; for the following 5 layers is 101 samples; and for the last layer is 51 samples. Overall, the network consists of 1,754,017 total parameters all of which are trainable. For the input layer and the convolutional layers, we use the rectified linear unit (ReLU) activation function, σ , (Ekman, 2021) which computes the function $\sigma(x) = \max(0, x)$. We use a stochastic gradient descent optimization algorithm with momentum along with the mean-squared loss function as the objective function Géron (2019). To prevent the network from over-fitting, we split the input data into training data set, testing data set, and validation data set using 60%, 20%, and 20% ratios, respectively.

For the training model selection, we use the Marmousi (Versteeg, 1994) and Pluto (Stoughton et al., 2001) velocity models. For the training source and receiver geometry, we use the source and receiver geometry of the field data set. We extract sub-models from the Marmousi and Pluto models and add a water layer to the top of each model using the water column depth of the field data set. For each velocity model, we use a density model that is a scaled version of the velocity model by a factor of two (and the units are converted from km/s to g/cm³) and has the same water layer as the velocity models. Scaling the velocity model by two and adding the water layer into the density model creates a range of reflection coefficients for training purposes that helps generalize the network applicability. We use 52 input shot gathers with free-surface multiples and ghost reflections each of which consists of 100 traces (total of 5,200 input traces) using 2D finite-difference forward modeling, and 52 output shot gathers without free-surface multiples and ghost reflections each of which consists of 100 traces (total of 5,200 output traces) using 2D finite-difference forward modeling.

FIELD DATA EXPERIMENT: THE MOBIL AVO VIKING GRABEN

DATA SET FROM THE NORTH VIKING GRABEN

The Mobil AVO Viking Graben data set was acquired in the North Sea over the Viking Graben (Keys and Foster, 1998). The initial purpose of this data set was to test different AVO methods using a single data set, however, when the results were presented at a workshop at the 64th SEG International Exposition and Annual Meeting in 1994, this data set was also used to cover problems related to geology, inversion, data processing, wave propagation, rock properties, and AVO (Lumley et al., 1998; Keys and Foster, 1998).

The seismic line consists of 1001 shot gathers each of which has a 6 s recording length with a 4 ms sampling rate. For each shot gather, 120 receivers are used, and the near-offset receiver is located at 262 m and the far-offset receiver is located at 3,237 m. Both the shot and receiver group interval is 25 m. The receivers are placed at a 10 m depth, and the air-gun array is placed at a 6 m depth (Keys and Foster, 1998).

The study area has a water depth of approximately 350 m. Strong water-bottom and interbed multiples contaminate the data and are a major source of noise (Keys and Foster, 1998; Madiba and McMechan, 2003). We use a CNN-based algorithm to attenuate free-surface multiples and ghost reflections, simultaneously, from this data set.

[Figure 2 about here.]

As part of the pre-processing of the seismic data for the CNN application, we first account for the geometric spreading in both the field data set and the synthetic data set used for training. The 3D effects of geometric spreading (Liner, 2016) can be accounted for by

$$A_{3D} \propto \frac{1}{t}, \quad (3)$$

and similarly, the 2D effects of geometric spreading (Liner, 2016) can be accounted for by

$$A_{2D} \propto \frac{1}{\sqrt{t}}, \quad (4)$$

where A denotes the amplitude and t denotes time. Therefore, we apply a t gain and \sqrt{t} gain to the field data set and the synthetic data set, respectively. Because we use 1D convolutional layers, we mimic the amplitudes in 1D by applying the geometric spreading corrections given in equations (3) and (4). Next, we apply a band-pass filter with 15 Hz and 50 Hz cuts to the field data set to match the frequency content of the training data set and the field data set. We also normalize the data prior to using for the CNN application (Géron, 2019; Ekman, 2021). As a last step of the pre-processing, we only use the first three seconds of the seismic data for computational efficiency purposes.

Figure 2(a) shows the raw shot gather number 88 from the field data set and following the pre-processing steps described above, Figure 2(b) shows the shot gather shown in Figure 2(a) after applying t gain, band-pass filter, and keeping the data recorded from 0 s to 3 s only.

[Figure 3 about here.]

After applying the pre-processing steps to the entire field data set, we apply the CNN-based free-surface multiple attenuation and seismic deghosting. Figure 3(a) shows the shot gather number 88 before free-surface multiple attenuation and seismic deghosting. Figure 3(b) shows the shot gather number 88 after free-surface multiple attenuation and seismic

deghosting using a CNN. The red arrows in Figure 3(a) indicate some of the 1st- and 2nd-order free-surface multiples and the red arrows in Figure 3(b) point to areas in the data where these multiples have been attenuated.

[Figure 4 about here.]

Figure 4(a) shows the near-offset trace of each shot gather (or the near-trace gather) of the entire data set before free-surface multiple attenuation and seismic deghosting, and Figure 4(b) shows the near-trace gather of the entire data set after free-surface multiple attenuation and seismic deghosting. The red arrows between 1 s and 1.2 s on the left and right sides in Figure 4(a) point to the 1st-order free-surface multiples, and the three red arrows between 1.5 s and 1.7 s on the left side in Figure 4(a) point to the 2nd-order free-surface multiples. Figure 4(b) shows that these multiples have been attenuated by our CNN-based algorithm.

[Figure 5 about here.]

To better evaluate the CNN prediction, we use auto-correlation plots as a diagnostic for periodicity in the records that is associated with multiples (Yilmaz, 2001). Figure 5(a) shows the auto-correlation of the near-trace gather shown in Figure 4(a) before free-surface multiple attenuation and seismic deghosting. Figure 5(b) shows the auto-correlation of the near-trace gather shown in Figure 4(b) after free-surface multiple attenuation and seismic deghosting. The red arrows around 0.5 s and 1 s in Figure 5(a) indicate the periodicity of the 1st- and 2nd-order free-surface multiples, respectively. Figure 5(b) shows that both 1st- and 2nd-order free-surface multiples have been attenuated and their periodicity is not evident in the auto-correlation of the data after the application of our CNN-based algorithm.

Next, we evaluate the CNN-prediction results for seismic deghosting by comparing the average amplitude spectra before and after CNN-based free-surface multiple attenuation and seismic deghosting using the near-trace gathers shown in Figure 4. Figure 5(c) shows the average amplitude spectrum before free-surface multiple attenuation and seismic deghosting (red line) using the near-trace gather shown in Figure 4(a), and the average amplitude spectrum after free-surface multiple attenuation and seismic deghosting (blue line) using the near-trace gather shown in Figure 4(b). The average amplitude spectra before and after deghosting in Figure 5(c) show that the low frequencies have been recovered as a result of the CNN-based seismic deghosting.

[Figure 6 about here.]

Next, we use common depth point (CDP) gathers to evaluate the effectiveness of our CNN-based free-surface multiple attenuation. We first apply a normal-moveout correction (NMO) to the CDP gathers using a 1D velocity profile (Keys and Foster, 1998). Because multiples have a slower velocity than the actual medium velocity, they appear on the NMO-corrected gathers as not flattened completely (or under-corrected), and the NMO-corrected CDP gathers help us distinguish between the primary and multiple reflections (Yilmaz, 2001). Figure 6(a) shows NMO-corrected 700th CDP before free-surface multiple attenuation and deghosting, and Figure 6(b) shows NMO-corrected 700th CDP after free-surface multiple attenuation and deghosting using the CNN. The red arrows in Figure 6(a) indicate some of the under-corrected multiples, and Figure 6(b) shows that those multiples have been attenuated. We also mute the NMO-corrected gathers in Figure 6 for the stretch zones at large offsets.

[Figure 7 about here.]

We sum the traces in the NMO-corrected CDP gathers, which is referred to as CDP stacking, to obtain a stack trace at the particular CDP location. The CDP stacking attenuates multiples to some extent as a result of residual moveout after applying NMO correction (Yilmaz, 2001). The CDP stack sections of the entire seismic data set after applying AGC with 500 ms time gate (Yilmaz, 2001) for display purposes before and after the attenuation of surface multiples and deghosting with the CNN are shown in Figure 7(a) and Figure 7(b), respectively. The red arrow in Figure 7(a) indicates free-surface multiples after CDP stacking using the data before free-surface multiple attenuation, and as shown in Figure 7(b), these multiples are attenuated by the application of the CNN. The events in Figure 7(a) are more continuous than the reflectors in Figure 7(b). Comparing the areas pointed out by the red ellipses in Figure 7, the free-surface multiples that mask the primary reflection have been removed and the continuity of the primary has been recovered after attenuating the free-surface multiples and removing the ghost reflections using the CNN.

[Figure 8 about here.]

Lastly, Figure 8 shows the auto-correlation of the CDP stack section before and after free-surface multiple attenuation by the CNN in Figure 8(a) and Figure 8(b), respectively. The red arrows in Figure 8(a) point out the remaining free-surface multiples after CDP stacking, and as shown in Figure 8(b), these remaining multiples have been attenuated by the application of our CNN-based algorithm.

CONCLUSIONS

We apply a CNN-based free-surface multiple attenuation and seismic deghosting to the Mobil AVO Viking Graben data set. Our CNN-based solution applies a trace-by-trace at-

tenuation of free-surface multiples and ghost removal, and does not rely on a dense spatial distribution of sources and receivers. Therefore, our CNN-based method is suitable for acquisition geometries with irregular and sparse sources and receivers, and the accuracy of the prediction does not rely upon the availability of the near-offset and neighboring traces (which is one of the important requirements for the conventional SRME and deghosting algorithms). We show that while our CNN-based method removes the effects of free-surface (i.e., free-surface multiples and ghost reflections), it also preserves and increases the continuity of the primary reflections in the seismic data. We show that the 1st- and 2nd-order free-surface multiples have been successfully attenuated and the low-frequency content of the seismic data has been successfully recovered.

ACKNOWLEDGEMENTS

We thank Khalid Almuteri from the Center for Wave Phenomena (CWP) for his help with the CNN setup and fruitful discussions. This work is supported by the Consortium Project on Seismic Inverse Methods for Complex Structures at the Colorado School of Mines. The finite-difference forward modeling examples in this paper were generated using the Madagascar software package Fomel et al. (2013). Machine learning implementations were completed using the TensorFlow source library (<https://www.tensorflow.org/>).

DATA AND MATERIALS AVAILABILITY

Data associated with this research are publicly available and can be obtained by visiting https://wiki.seg.org/wiki/Mobil_AVO_viking_graben_line_12.

REFERENCES

- Almuteri, K., and P. Sava, 2021, A convolutional neural network approach for ghost removal: First International Meeting for Applied Geoscience & Energy Expanded Abstracts, 2550–2554.
- Amundsen, L., and H. Zhou, 2013, Low-frequency seismic deghosting: *GEOPHYSICS*, **78**, WA15–WA20.
- Bishop, C. M., 2006, *Pattern Recognition and Machine Learning*: Springer.
- Carlson, D. H., A. Long, W. Sollner, H. Tabti, R. Tenghamn, and N. Lunde, 2007, Increased resolution and penetration from a towed dual-sensor streamer: *First Break*, **25**, 71–77.
- Dondurur, D., 2018, *Acquisition and Processing of Marine Seismic Data*: Elsevier.
- Dragoset, B., E. Verschuur, I. Moore, and R. Bisley, 2010, A perspective on 3D surface-related multiple elimination: *GEOPHYSICS*, **75**, 75A245–75A261.
- Ekman, M., 2021, *Learning deep learning: Theory and practice of neural networks, computer vision, NLP, and transformers using TensorFlow*: Addison-Wesley Professional.
- Fomel, S., P. Sava, I. Vlad, Y. Liu, and V. Bashkardin, 2013, Madagascar: open-source software project for multidimensional data analysis and reproducible computational experiments: *Journal of Open Research Software*, **1**, e8.
- Géron, A., 2019, *Hands-on machine learning with Scikit-Learn, Keras, and TensorFlow*, 2nd edition: O’Reilly Media, Inc.
- Hu, Y., R. Zhen, and H. Sheikh, 2019, Cnn-based deghosting in high dynamic range imaging: 2019 IEEE International Conference on Image Processing (ICIP), 4360–4364.
- Keys, R. G., and D. J. Foster, 1998, Comparison of Seismic Inversion Methods on a Single Real Data Set: 1. A Data Set for Evaluating and Comparing Seismic Inversion Methods: *Society of Exploration Geophysicists*, 1–12.

- Kiraz, M. S. R., R. Snieder, and J. Sheiman, 2023, Removing the effects of free-surface from seismic data using convolutional neural networks – Part 1: Theory and sensitivity analysis: *to be submitted to GEOPHYSICS*.
- Kragh, E., E. Muyzert, T. Curtis, M. Svendsen, and D. Kapadia, 2010, Efficient broadband marine acquisition and processing for improved resolution and deep imaging: The Leading Edge, **29**, 464–469.
- Liner, C. L., 2016, Elements of 3D Seismology, Third edition: Chapter 1: General Properties of Waves, 3–16.
- Liu-Rong, T., J. Jin-Sheng, R. Hao-Ran, Y. Yue-Ming, and W. Bang-Yu, 2021, The separation of seismic surface-related multiples based on CAE-SAGAN: First International Meeting for Applied Geoscience & Energy Expanded Abstracts, 2914–2918.
- Lumley, D. E., D. Nichols, C. Ecker, T. Rekdal, and A. Berlioux, 1998, Comparison of Seismic Inversion Methods on a Single Real Data Set: 5. Amplitude-Preserved Processing and Analysis of the Mobil AVO Data Set: Society of Exploration Geophysicists, 75–96.
- Madiba, G. B., and G. A. McMechan, 2003, Processing, inversion, and interpretation of a 2D seismic data set from the North Viking Graben, North Sea: GEOPHYSICS, **68**, 837–848.
- Moldoveanu, N., L. Combee, M. Egan, G. Hampson, L. Sydora, and W. Abriel, 2007, Over/under towed-streamer acquisition: A method to extend seismic bandwidth to both higher and lower frequencies: The Leading Edge, **26**, 41–58.
- Ovcharenko, O., A. Baumstein, and E. Neumann, 2021, Surface-related multiple elimination through orthogonal encoding in the latent space of convolutional autoencoder: First International Meeting for Applied Geoscience & Energy Expanded Abstracts, 1355–1359.
- Plessix, R.-E., 2006, A review of the adjoint-state method for computing the gradient of a

- functional with geophysical applications: *Geophysical Journal International*, **167**, 495–503.
- Siahkoohi, A., M. Louboutin, R. Kumar, and F. J. Herrmann, 2018, Deep-convolutional neural networks in prestack seismic: Two exploratory examples: *SEG Technical Program Expanded Abstracts*, 2196–2200.
- Siahkoohi, A., D. J. Verschuur, and F. J. Herrmann, 2019, Surface-related multiple elimination with deep learning: *SEG Technical Program Expanded Abstracts*, 4629–4634.
- Soubaras, R., 2010, Deghosting by joint deconvolution of a migration and a mirror migration: *SEG Technical Program Expanded Abstracts*, 3406–3410.
- Soubaras, R., and P. Whiting, 2011, Variable depth streamer - the new broadband acquisition system: *SEG Technical Program Expanded Abstracts*, 4349–4353.
- Stoughton, D., J. Stefani, and S. Michell, 2001, 2D elastic model for wavefield investigations of subsalt objectives, deep water Gulf of Mexico: *SEG Technical Program Expanded Abstracts*, 1269–1272.
- Tarantola, A., 1984, Inversion of seismic reflection data in the acoustic approximation: *GEOPHYSICS*, **49**, 1259–1266.
- Verschuur, D. J., A. J. Berkhout, and C. P. A. Wapenaar, 1992, Adaptive surface-related multiple elimination: *GEOPHYSICS*, **57**, 1166–1177.
- Versteeg, R., 1994, The Marmousi experience: Velocity model determination on a synthetic complex data set: *The Leading Edge*, **13**, 927–936.
- Vrolijk, J.-W., and G. Blacquière, 2021, Source deghosting of coarsely sampled common-receiver data using a convolutional neural network: *GEOPHYSICS*, **86**, V185–V196.
- Yilmaz, O., 2001, *Seismic Data Analysis*: Society of Exploration Geophysicists.
- Zhang, D., M. de Leeuw, and E. Verschuur, 2021, Deep learning-based seismic surface-

related multiple adaptive subtraction with synthetic primary labels: First International Meeting for Applied Geoscience & Energy Expanded Abstracts, 2844–2848.

LIST OF FIGURES

1	Schematic illustration of the ray paths of primary reflection (blue line), free-surface multiple (black line), and source- and receiver-side ghost reflections (red line). The white triangle denotes a receiver located at depth and the red shape denotes a source located at depth.	19
2	(a) Raw shot gather. (b) Shot gather in (a) after applying the pre-processing steps.	20
3	(a) Shot gather <i>before</i> free-surface multiple attenuation and deghosting. (b) Shot gather <i>after</i> free-surface multiple attenuation and deghosting using the CNN-based algorithm.	21
4	(a) Near-trace gather of the seismic line <i>before</i> free-surface multiple attenuation and deghosting shown only 0-2 s. (b) Near-trace gather of the seismic line <i>after</i> free-surface multiple attenuation and deghosting using a CNN shown only 0-2 s.	22
5	(a) Auto-correlation of the near-trace gather <i>before</i> free-surface multiple attenuation and deghosting shown in Figure 4(a). (b) Auto-correlation of the near-trace gather <i>after</i> free-surface multiple attenuation and deghosting shown in Figure 4(b). (c) Amplitude spectra of the near-trace gather <i>before</i> (red line) and <i>after</i> (blue line) free-surface multiple attenuation and deghosting.	23
6	(a) NMO-corrected CDP gather <i>before</i> free-surface multiple attenuation and deghosting after muting the stretch zone. (b) NMO-corrected CDP gather <i>after</i> free-surface multiple attenuation and deghosting after muting the stretch zone.	24
7	(a) CDP stack <i>before</i> free-surface multiple attenuation and deghosting after applying AGC. (b) CDP stack <i>after</i> free-surface multiple attenuation and deghosting after applying AGC.	25
8	(a) Auto-correlation of the near-trace gather <i>before</i> free-surface multiple attenuation and deghosting shown in Figure 7(a). (b) Auto-correlation of the near-trace gather <i>after</i> free-surface multiple attenuation and deghosting shown in Figure 7(b).	26

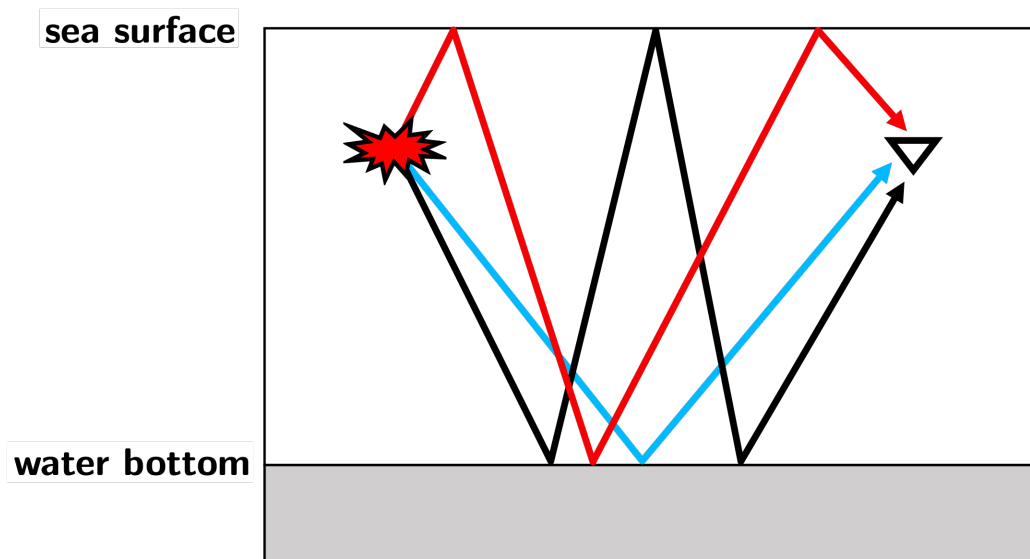


Figure 1: Schematic illustration of the ray paths of primary reflection (blue line), free-surface multiple (black line), and source- and receiver-side ghost reflections (red line). The white triangle denotes a receiver located at depth and the red shape denotes a source located at depth.

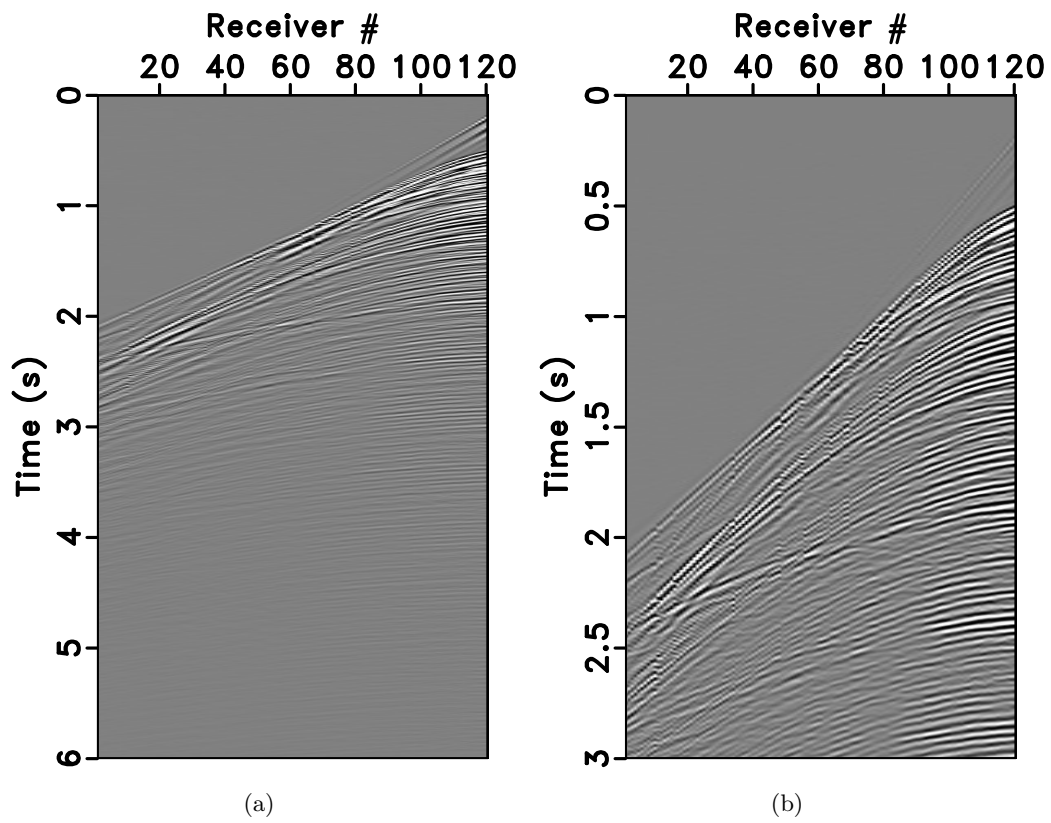


Figure 2: (a) Raw shot gather. (b) Shot gather in (a) after applying the pre-processing steps.

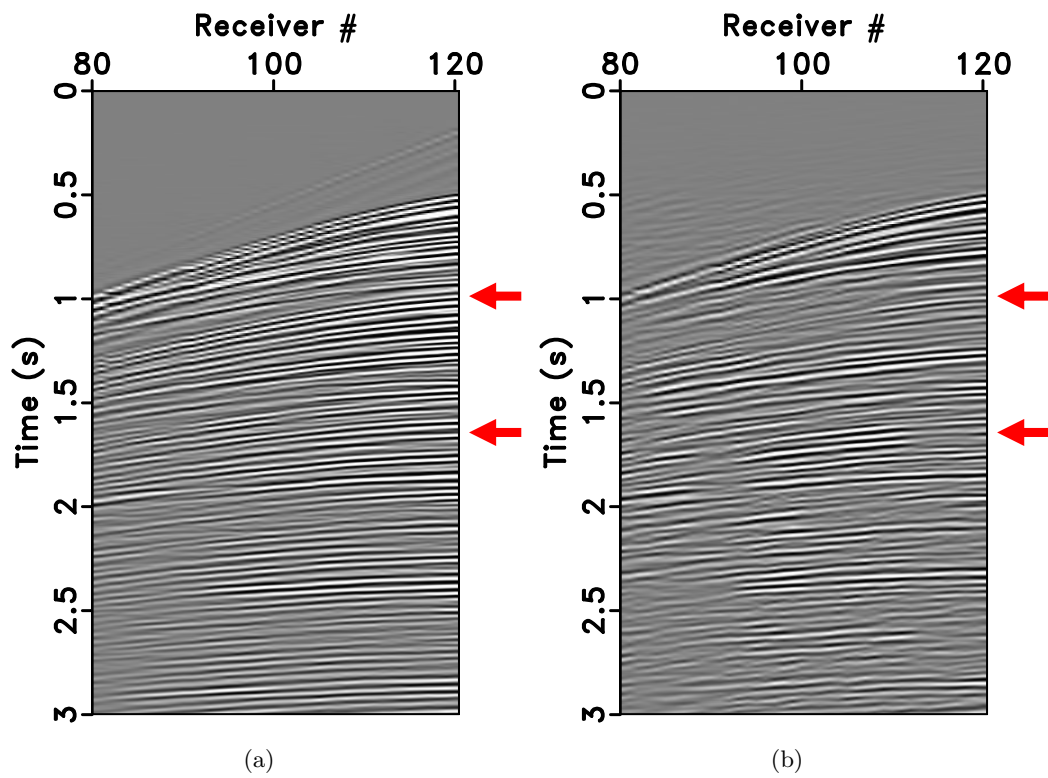
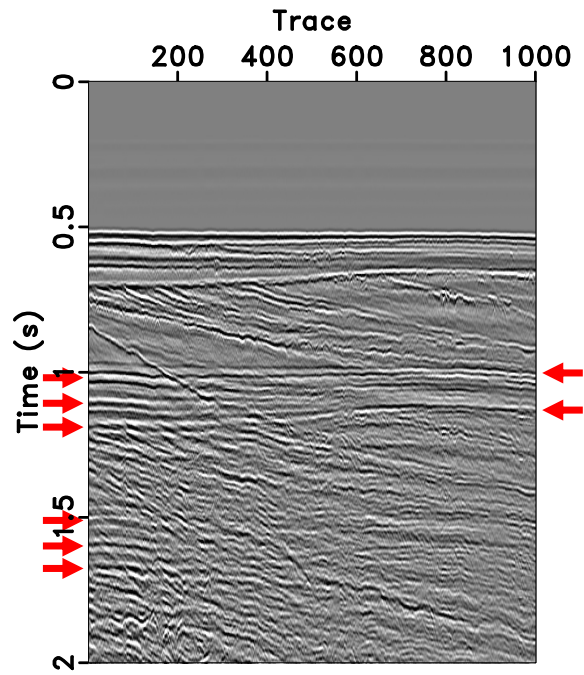
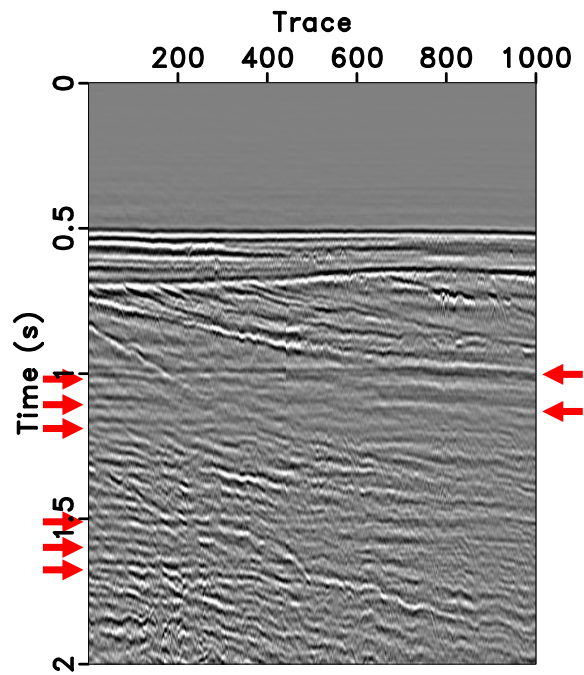


Figure 3: (a) Shot gather *before* free-surface multiple attenuation and deghosting. (b) Shot gather *after* free-surface multiple attenuation and deghosting using the CNN-based algorithm.



(a)



(b)

Figure 4: (a) Near-trace gather of the seismic line *before* free-surface multiple attenuation and deghosting shown only 0-2 s. (b) Near-trace gather of the seismic line *after* free-surface multiple attenuation and deghosting using a CNN shown only 0-2 s.

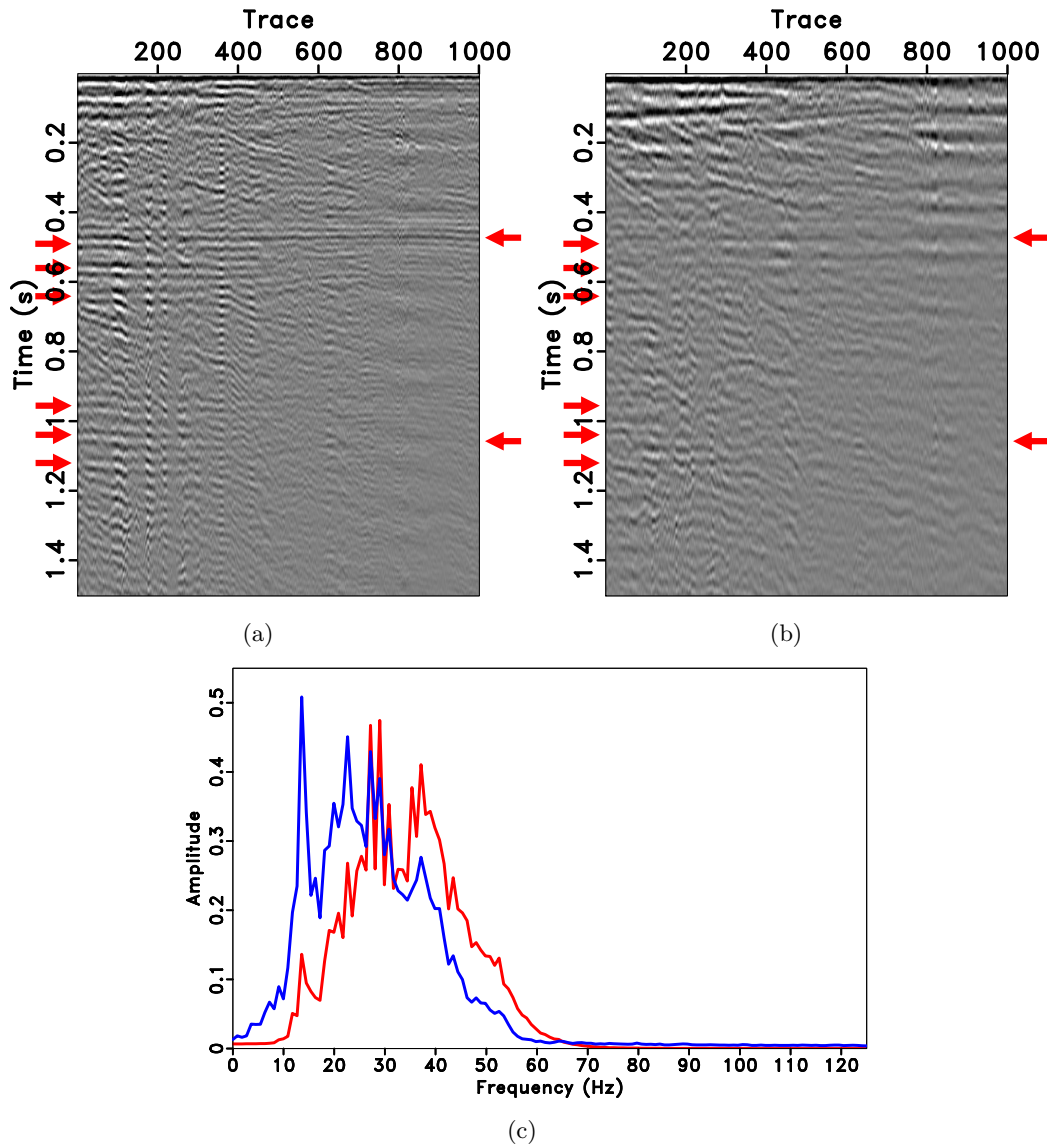
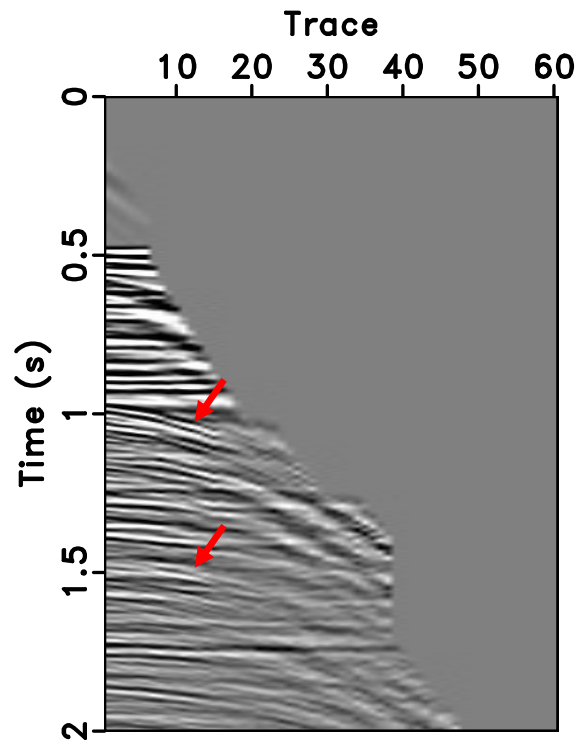
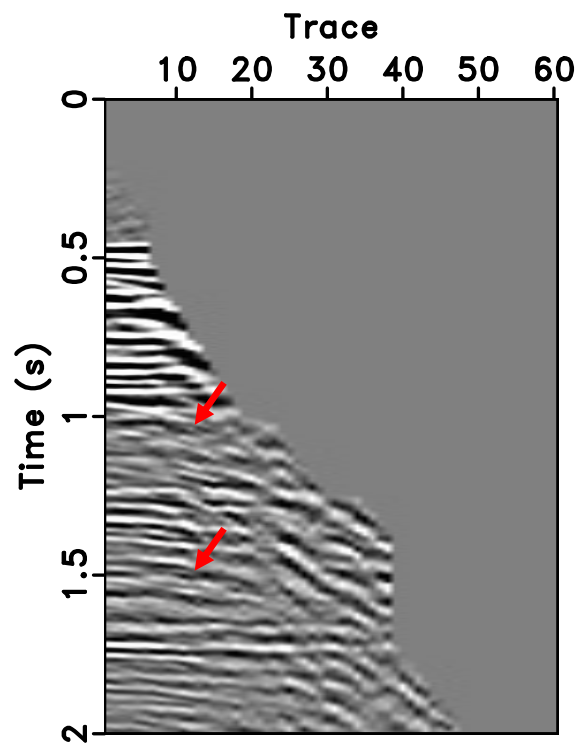


Figure 5: (a) Auto-correlation of the near-trace gather *before* free-surface multiple attenuation and deghosting shown in Figure 4(a). (b) Auto-correlation of the near-trace gather *after* free-surface multiple attenuation and deghosting shown in Figure 4(b). (c) Amplitude spectra of the near-trace gather *before* (red line) and *after* (blue line) free-surface multiple attenuation and deghosting.

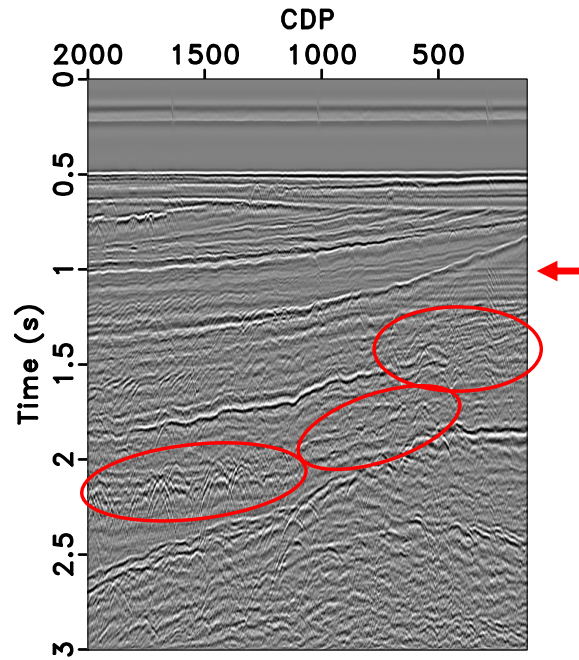


(a)

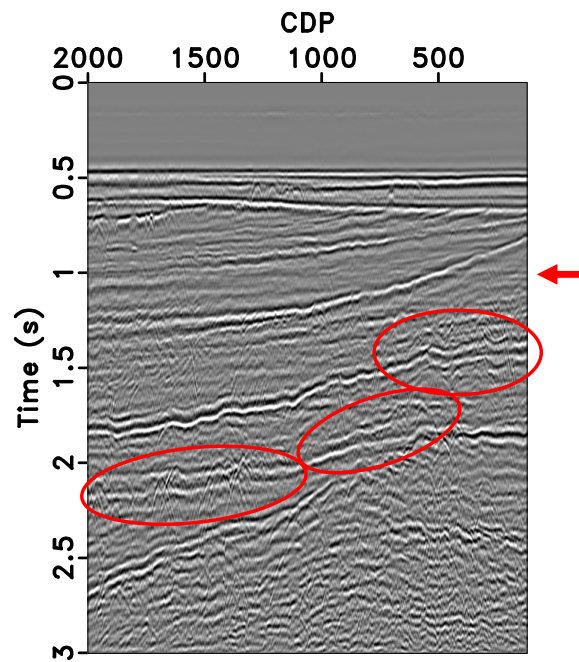


(b)

Figure 6: (a) NMO-corrected CDP gather *before* free-surface multiple attenuation and deghosting after muting the stretch zone. (b) NMO-corrected CDP gather *after* free-surface multiple attenuation and deghosting after muting the stretch zone.

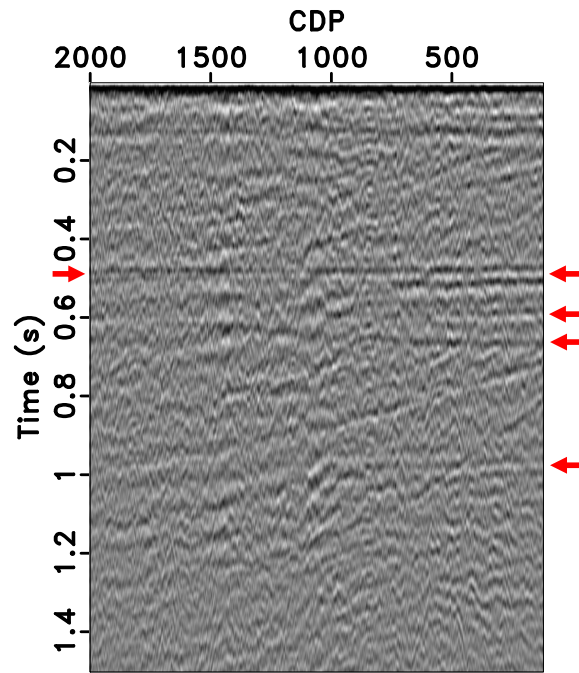


(a)

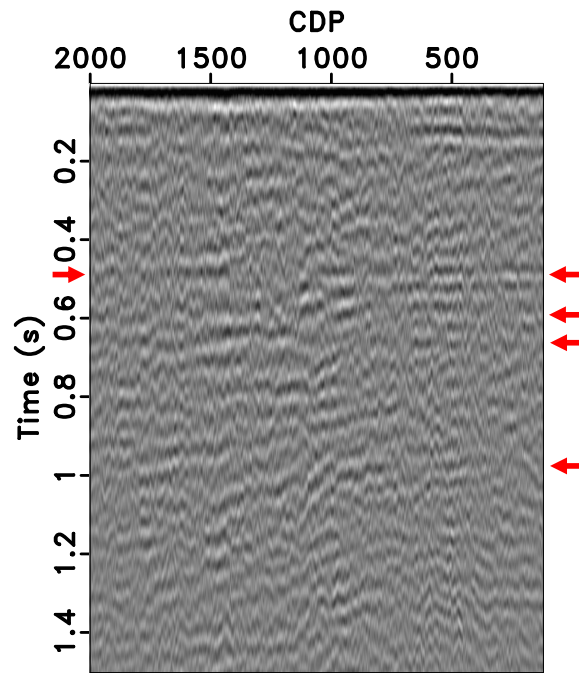


(b)

Figure 7: (a) CDP stack *before* free-surface multiple attenuation and deghosting after applying AGC. (b) CDP stack *after* free-surface multiple attenuation and deghosting after applying AGC.



(a)



(b)

Figure 8: (a) Auto-correlation of the near-trace gather *before* free-surface multiple attenuation and deghosting shown in Figure 7(a). (b) Auto-correlation of the near-trace gather *after* free-surface multiple attenuation and deghosting shown in Figure 7(b).